Received 24 October 2022; accepted 26 October 2022. Date of publication 31 October 2022; date of current version 8 November 2022.
The review of this article was arranged by Editor C. C. McAndrew.

Digital Object Identifier 10.1109/JEDS.2022.3218002

The Drift Region Width Modulation Technique for Breakdown Performance Enhancement of AlGaN/GaN HEMT

JIANHUA LIU[1,2], JUN ZHANG[1,2] (Member, IEEE), JIAFEI YAO[1,2] (Member, IEEE), MAN LI[1,2], JING CHEN[1,2], MAOLIN ZHANG[1,2], XIAOMING HUANG[1,2], CHENYANG HUANG[1,2], WEIHUA TANG[1,2] (Member, IEEE), AND YUFENG GUO[1,2] (Member, IEEE)

1 College of Integrated Circuit Science and Engineering, Nanjing University of Posts and Telecommunications, Nanjing 210023, China
2 National and Local Joint Engineering Laboratory of RF Integration and Micro-Assembly Technology, Nanjing University of Posts and Telecommunications, Nanjing 210023, China

CORRESPONDING AUTHORS: Y. GUO and J. ZHANG (e-mail: yfguo@njupt.edu.cn; bravaisxx@163.com)

This work was supported in part by the National Natural Science Foundation of China under Grant 61874059, Grant 61904083, and Grant 62074080; in part by the Natural Science Foundation of Jiangsu Province under Grant BK20190237, Grant BK20201206, and Grant BK20211104; and in part by the Postgraduate Research and Practice Innovation Program of Jiangsu Province under Grant 46006CX21713.

ABSTRACT The breakdown performance of the AlGaN/GaN high electron mobility transistor (HEMT) is limited by the high electric field peaks in the device. To obtain a more uniform electric field distribution, the drift region width modulation (DWM) technique is proposed to reshape the charge distribution between the gate and drain electrodes. By applying the Gaussian box method, an effective designing guidance for the structure optimization of the AlGaN/GaN HEMT with adaptive-width drift region pillars (AWD-HEMT) is obtained. The fabricated AWD-HEMT demonstrated a significant improvement in breakdown performance. The Baliga's figure of merit (BFOM) of AWD-HEMT improved 65.3% compared with the conventional HEMT, without introducing complicated processes. In addition, the mechanism of the AWD-HEMT is explored by numerical methods. The simulations indicate that a more uniform electric field distribution at AlGaN/GaN interfaces could be obtained, and the increased varying rate of the adaptive-width drift region (AWD) pillars results in a more obvious electric field modulation effect.

INDEX TERMS Electric field, breakdown voltage, adaptive-width drift region pillar, AlGaN/GaN HEMT.

I. INTRODUCTION

GaN is gaining increasing attention for its attractive performance in high frequency and high power applications resulting from its wide bandgap and high electron saturation mobility [1], [2], [3], [4]. Besides, profiting from the polarization-induced two-dimension electron gas (2DEG), the typical GaN-based power device, high electron mobility transistor (HEMT), could achieve high breakdown voltage (BV) and low specific on-resistance ($R_{on,sp}$) simultaneously [5], [6]. However, due to the electric field crowding effect, high electric field peaks emerge at the electrodes. The nonuniformly distributed electric field enhances the drain leakage current, hence limiting the device's BV. Intensive investigations have been devoted to pursuing higher breakdown performance. The field plate technique, as shown in Fig. 1(a), is employed to curb the excessive electric field peaks at electrodes [7], [8], [9], [10]. As demonstrated in Fig. 1(b), the gate width modulation technique is also an effective approach to mitigate the electric field peak at the edge of the gate electrode [11], [12]. The above techniques are employed to ease the electric field near the electrodes. However, the modulation of the electric field distribution in the whole drift region that between the gate and drain electrodes is still missing, leaving a vast space for devices' BV improvement.

Based on the charge-induced electric field modulation effect, the Variation Lateral Width (VLW) technique was firstly employed on Si-based power devices in 2015 [13], [14]. Same as other junction terminal techniques applied to Si-based power devices, these mature

This work is licensed under a Creative Commons Attribution 4.0 License. For more information, see https://creativecommons.org/licenses/by/4.0/

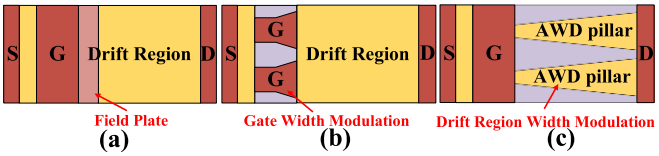

FIGURE 1. The top-view schematics of (a) the AlGaN/GaN HEMT with field plate, (b) the AlGaN/GaN HEMT with gate width modulation technique, and (c) the AlGaN/GaN HEMT with adaptive-width drift region pillars (AWD-HEMT).

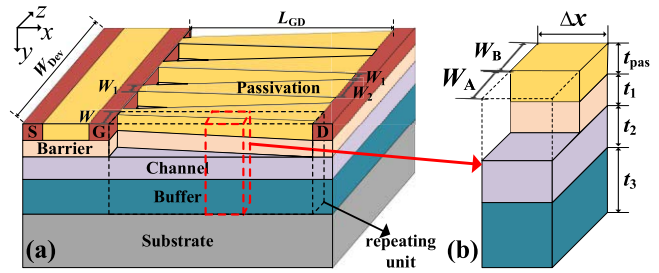

FIGURE 2. (a) The three-dimensional schematic of the AWD-HEMT and (b) the side-view schematic of the AWD-HEMT's Gaussian box in the repeating unit.

methodologies are unable to be transferred directly to the GaN-based power devices as a result of different structures and mechanisms. The Si-based VLW technique modulates the charge distribution by altering the physical structure of the silicon layer. While the drift region width modulation (DWM) technique proposed in this work realizes an improved breakdown performance by adjusting the 2DEG distribution without damaging the GaN channel layer as shown in Fig. 1 (c). The effectiveness of the proposed AWD-HEMT is verified by the measurements from fabricated devices. Moreover, the mechanism of the AWD-HEMT-induced breakdown performance enhancement is investigated by the simulation tool Synopsys Sentaurus TCAD. According to the simulation and experimental results, the DWM technique is an effective approach to achieving a more uniform electric field profile and an improved breakdown performance compared with the conventional HEMT.

II. DEVICE STRUCTURE

Fig. 2(a) shows the three-dimensional schematic of the AWD-HEMT. The total width of the device is denoted as W_{Dev}. The width of each adaptive-width drift region (AWD) pillar increases from the gate electrode to the drain electrode (W_1 to W_2), and the gap between the adjacent AWD pillars is set as W_1. In light of the 2DEG distribution being determined by the AWD pillars, the topologies of the AWD pillars are vital for the AWD-HEMT's breakdown characteristic. Considering the symmetrical and periodical natures of the AWD pillars, the characteristics of the device could be explored by the repeating units between gate and drain electrodes as shown in Fig. 2(a). Therefore, the Gaussian box of the width Δx as shown in Fig. 2(b) with red dash cuboid is applied to provide physical insights of the breakdown mechanism in AWD-HEMT. The Gaussian box includes the buffer layer, the channel layer, the barrier layer and the passivation layer as shown in Fig. 2(b). Here, W_{A} is the width of the etched region with the permittivity of $\varepsilon_{\mathrm{Air}}$. W_{B} is the width of the barrier layer with the permittivity of ε_1. $W = W_{\mathrm{A}}+W_{\mathrm{B}}$ is the width of a repeating unit. ε_2 is the permittivity of the GaN channel and buffer layer. Considering the natural boundary condition of the GaN HEMT that the vertical electric field at both of the passivation surface and buffer bottom ought to be near zero, the electric flux passing through the top and bottom of the Gaussian box could be neglected. There is also no electric flux passing through the Gaussian box along the z-direction owing to the symmetry and periodicity [13]. Therefore, the Gaussian law in the box could be expressed as Eq. (1).

$$\begin{aligned}&(W_{\mathrm{A}}C_{\mathrm{Air}} + W_{\mathrm{B}}C_{\mathrm{Pas}})\varphi \\ &\quad + [(W_{\mathrm{A}}\varepsilon_{\mathrm{Air}} + W_{\mathrm{B}}\varepsilon_1)t_1 + W\varepsilon_2 t_2 + W\varepsilon_2 t_3]\frac{dE}{dx} \\ &\quad \approx q(N_1 t_1 + \sigma)W_{\mathrm{B}} + q(N_2 t_2 - Pt_3)W \end{aligned} \tag{1}$$

The concentrations and thicknesses of the barrier layer, channel layer and buffer layer are denoted as N_1, N_2, P, t_1, t_2 and t_3 respectively. Here, the buffer layer is assumed as the p-type GaN considering the existence of the acceptor-like traps [15], [16], [17]. q is the electric charge. σ is the polarization sheet charge concentration. C_{Air} and C_{Pas} are the specific capacitance of the air and passivation layer. E and φ are assumed as the electric field and potential in the box for simplicity. In Eq. (1), the first term on the left-hand side is the electric flux passing through the Gaussian box, and the second term is the electric flux into the Gaussian box along the x-direction. For an optimized AWD-HEMT, the ideal case is the electric field in the Gaussian box being constantly equal to the critical electric field of GaN (E_C). So that the ideal breakdown performance of the device can be achieved [13], [18]. Thus, the potential in the Gaussian box is $\varphi = Ex$, when the breakdown occurs. However, due to the non-ideal material quality and inherent 2-D coupling effects, the ideal electric field could not be achieved in real-world devices. Therefore, the average electric field could be applied to replace the critical electric field. Therefore, W_{B} could be derived as Eq. (2). Here, $Q_1 = qN_1t_1$, $Q_2 = qN_2t_2$, $Q_3 = qPt_3$ and $Q_\sigma = q\sigma$ are denoted as the sheet charge density of the barrier layer, channel layer, buffer layer and the 2DEG respectively.

$$W_{\mathrm{B}} \approx W(E_{\mathrm{C}}C_{\mathrm{Air}}x + Q_3 - Q_2)/[Q_1 + Q_\sigma - E_{\mathrm{C}}(C_{\mathrm{Pas}} - C_{\mathrm{Air}})x] \tag{2}$$

Since the Q_1+Q_σ is far larger than E_{C}(C_{Pas}-C_{Air})L_{GD}, and L_{GD}>x. The Eq. (2) could be simplified as Eq. (3).

$$W_{\mathrm{B}} \approx WE_{\mathrm{C}}C_{\mathrm{Air}}x/(Q_1 + Q_\sigma) + W(Q_3 - Q_2)/(Q_1 + Q_\sigma) \tag{3}$$

The Eq. (3) indicates that a linear W_B, Q_1, Q_2, Q_3, and Q_σ along the x-direction could ensure the uniform electric field. In other words, to achieve a uniformly distributed electric field, the width of AWD pillar ought to be linearly

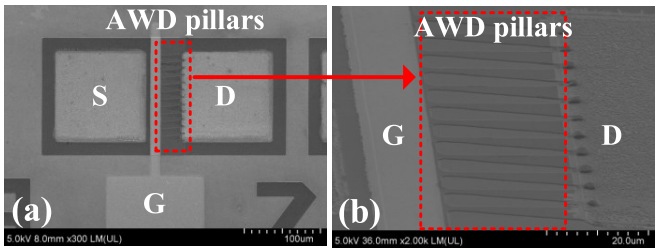

FIGURE 3. The SEM micrographs of (a) the fabricated AWD-HEMT and (b) the linear widened AWD pillars.

increased along the x direction. Theoretically speaking, the uniform electric field can also be obtained by altering the sheet charge density (Q_1, Q_2, Q_3, and Q_σ), which concept is successfully accepted and widely applied in Si-based power devices. Nevertheless, such an approach is difficult to be employed in GaN-based HEMTs as the doping process shall significantly reduce the material quality and therefore create a deteriorated performance in many aspects. Hence, the linear W_B is a promising approach to fulfill the Eq. (3) and is the first time proposed to modulate the electric field distribution in AlGaN/GaN HEMTs.

III. FABRICATION PROCESS

The HEMTs are fabricated on the AlGaN/GaN heterostructure sample composed of 20nm $Al_{0.25}Ga_{0.75}N$ layer, 200nm GaN channel layer and 2.5μm GaN buffer layer grown on <111> silicon substrate by metal-organic chemical vapor deposition. The passivation-prior-to-ohmic process is employed to suppress the formation of surface states and protect the AlGaN/GaN heterostructure from the damage and contamination of the following fabrication processes. The passivation layer comprises 3nm in-*situ* Si_3N_4 cap layer, 70nm Si_3N_4 grown by low-pressure chemical vapor deposition (LPCVD) and 130nm Si_3N_4 grown by plasma-enhanced chemical vapor deposition (PECVD). The LPCVD Si_3N_4 is employed for its high thermal stability and compact film quality [19]. The total width (W_{Dev}) of the fabricated device is 120μm. The device fabrication started with the mesa isolation accomplished by Inductively Coupled Plasma-Reactive Ion Etching (ICP-RIE) (CHF_3/O_2) to etch Si_3N_4 and ICP (BCl_3) to etch AlGaN and GaN. Then, the electrodes are patterned by the ICP-RIE. The devices are annealed at the 800°C for 50s in the N_2 ambient to form the ohmic contact following the Ti/Al/Ni/Au (25nm/150nm/50nm/20nm) e-beam evaporation at drain and source footprints. Then the Ni/Au (200nm/50nm) e-beam evaporation and lift-off process are employed to form the Schottky gate electrodes. Finally, partial of the Si_3N_4 and AlGaN in the drift region is etched by ICP-RIE and ICP processes for the formation of the AWD pillars. Fig. 3(a) and (b) show the SEM micrographs of the fabricated AWD-HEMT, and the linear widened AWD pillars could be observed between the gate and the drain electrodes.

IV. RESULTS AND DISCUSSION

According to the guidance obtained from the Gaussian box method, the AWD pillars' widths of the fabricated

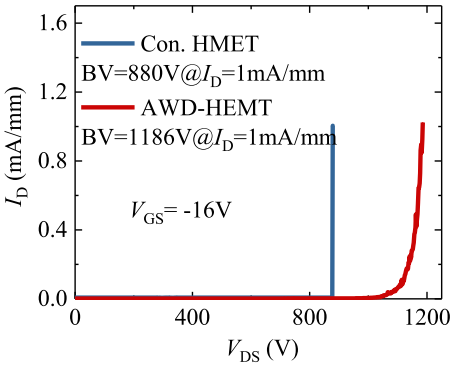

FIGURE 4. The experimental breakdown characteristics of the conventional HEMT and the AWD-HEMT (ratio = 4:1). (V_S = 0V, V_{GS} = −16V).

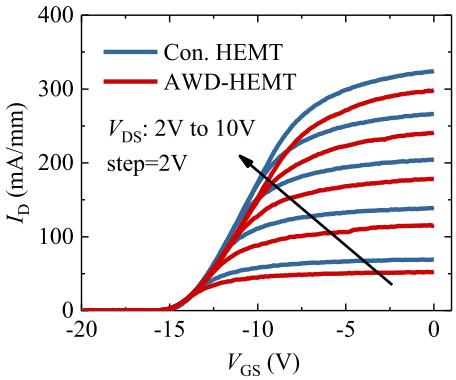

FIGURE 5. The experimental transfer characteristics of the conventional HEMT and the AWD-HEMT (ratio = 4:1). (V_S = 0V).

AWD-HEMTs increased linearly along the x-direction from the gate electrode to the drain electrode (Fig. 3). The ratio (W_2:W_1) indicates the varying rate of the AWD pillars' widths. Fig. 4 illustrates the breakdown characteristics of the conventional HEMT and the AWD-HEMT (ratio = 4:1). With the employment of the DWM technique, the BV of the device increased significantly, over 34.8%, from 880V to 1186V. The breakdown characteristics demonstrated in this work are measured by the devices immersed in Fluorinert FC-40 to avoid the influence of the air surrounding the top of the device [20], [21], [22], [23]. Fig. 5 shows the devices' transfer characteristics. The threshold voltage of the AWD-HEMT remains unchanged, compared with the conventional HEMT. As demonstrated in Fig. 5 and 6, the drain current of the transfer characteristics and output characteristics decreases slightly, resulting from the decrease of the 2DEG in the channel layer. Therefore, the $R_{on,sp}$ of the device increases by 9.9% with the increased ratio as shown in Fig. 7. Although the $R_{on,sp}$ degraded slightly, the BV and Baliga's figure of merit (BFOM) enhanced significantly, with 34.8% and 65.3% improvement respectively, as presented in Fig. 8 and Fig. 9.

To explore the mechanism of the BV and BFOM improvement as a result of AWD-HEMTs, the commercial TCAD

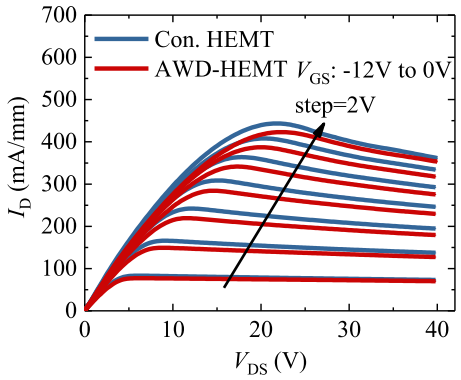

FIGURE 6. The experimental output characteristics of the conventional HEMT and the AWD-HEMT (ratio = 4:1). (V_S = 0V).

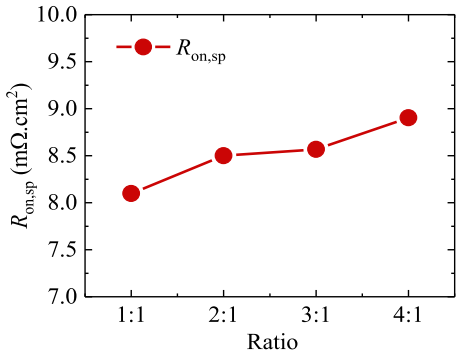

FIGURE 7. The experimental $R_{on,sp}$ of the conventional HEMT and the AWD-HEMTs with different ratios. (V_S = 0V, V_{GS} = 0V).

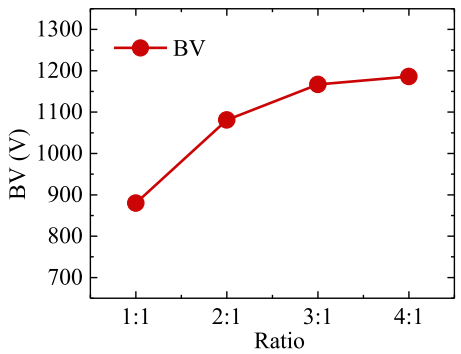

FIGURE 8. The experimental BV of the conventional HEMT and the AWD-HEMTs with different ratios. (V_S = 0V, V_{GS} = −16V).

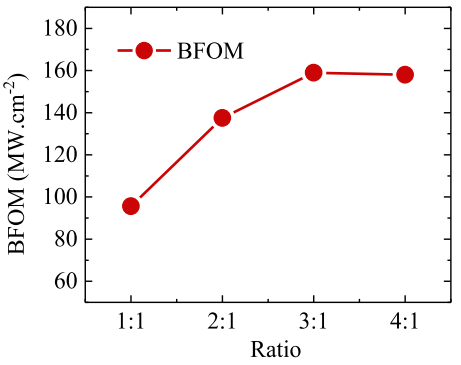

FIGURE 9. The experimental BFOM of the conventional HEMT and the AWD-HEMTs with different ratios. (V_S = 0V).

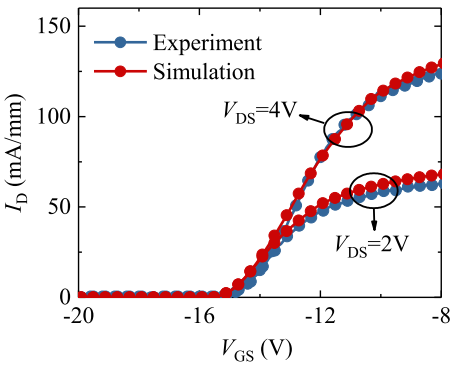

FIGURE 10. The calibrated simulation results versus experimental results for transfer characteristics of the conventional HEMT. (V_S = 0V).

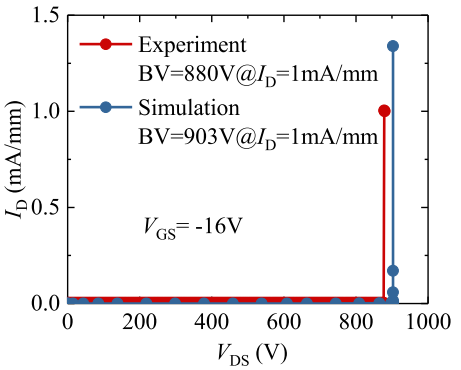

FIGURE 11. The calibrated simulation results versus experimental results for breakdown characteristics of the conventional HEMT. (V_S = 0V, V_{GS} = −16V).

tool Sentaurus is employed to conduct numerical simulation. First, to accurately analyze the physical nature of the proposed device, the calibration of the TCAD tool is required. As shown in Fig. 10 and 11, the measured transfer characteristics and breakdown characteristics of the conventional HEMT is used. A good agreement between simulation and experimental results can be achieved. The materials employed in the simulation are in accordance with the fabricated devices, including silicon substrate, GaN buffer, GaN channel, AlGaN barrier and Si_3N_4 passivation. The substitutional impurity of oxygen at the nitrogen site induced by ICP-RIE (CHF_3/O_2) acts as shallow donors [24], [25]. The effect of etch-induced damage is simulated by introducing electrons under the gate contact. The key parameters employed in the numerical simulation are shown in Table 1. The basic semiconductor equations, such as Poisson, drift-diffusion and current-continuity equations are included in the numerical simulation. The physical parameter models contain Shockley-Read-Hall, thermal dynamic model, high field-dependent mobility model, polarization model, carrier statistic model and tunneling model at the ohmic contacts.

As illustrated in Fig. 12, the electron distribution at the AlGaN/GaN heterojunction interface of the

TABLE 1. Key parameters employed in numerical simulation.

Symbol	Description	Value
x	Al mole fraction	0.25
t_{pas} (μm)	Thickness of Si_3N_4 passivation layer	0.2
t_1 (μm)	Thickness of AlGaN barrier layer	0.02
t_2 (μm)	Thickness of GaN channel layer	0.2
L_{GD} (μm)	Gate to drain distance	8
N_0 (cm^{-3})	Concerntration of etch-induced donors	2×10^{19}
N_1 (cm^{-3})	Doping concerntration of barrier layer	8×10^{18}
N_2 (cm^{-3})	Doping concerntration of channel layer	1×10^{16}

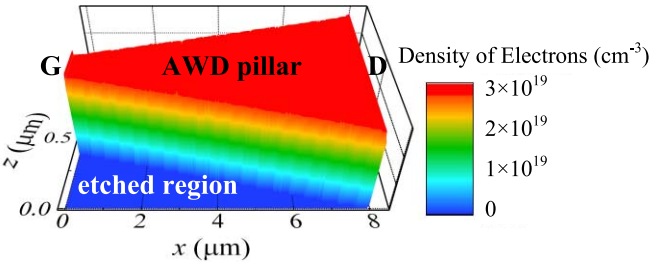

FIGURE 12. The electron distribution at the AlGaN/GaN heterojunction interface of the AWD-HEMT (ratio = 4:1). ($V_S = V_{GS} = V_{DS} = 0V$).

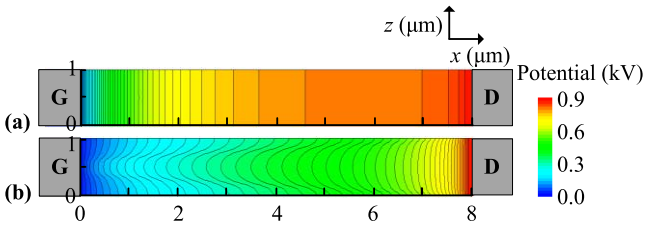

FIGURE 13. The potential distribution and equipotential contours at the AlGaN/GaN heterojunction interface of (a) the conventional HEMT and (b) the AWD-HEMT (ratio = 4:1). ($V_S = 0V$, $V_{GS} = -16V$, $V_{DS} = 900V$).

device is reshaped by employing the DWM technique ($V_S = V_{GS} = V_{DS} = 0V$). The potential distribution of the devices under the same bias ($V_S = 0V$, $V_{GS} = -16V$, $V_{DS} = 900V$) is modulated accordingly as shown in Fig. 13(a) and (b). In other words, a more uniform equipotential contour could be obtained with the DWM technique. The electric field distribution at the AlGaN/GaN heterojunction interface is the main concern for the BV optimization, as the device's breakdown tends to occur at the heterojunction. The electric field crowding at the gate electrode is eased as shown in Fig. 14(a) and (b). The drift regions of the HEMTs are fully depleted and the electric field modulation effect becomes more significant with the increased ratio.

Fig. 15 illustrates the BV versus $R_{on,sp}$ for AWD-HEMTs and other HEMTs in the published literature [26], [27], [28], [29], [30], [31]. AWD-HEMT presents a better breakdown performance in spite of a large $R_{on,sp}$. However, considering the good compatibility of the proposed method possessed, the $R_{on,sp}$ can be reduced by adopting other technologies such as multi-channel epitaxy or ohmic contact optimization. Fig. 16 shows that the AWD-HEMT presents an excellent

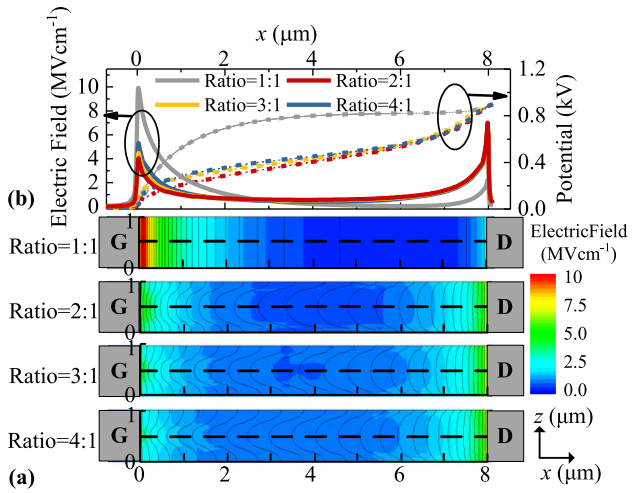

FIGURE 14. (a) The electric field distribution at the AlGaN/GaN heterojunction interface of the conventional HEMT and the AWD-HEMTs with different ratios. (b) The electric field distribution and the potential distribution at the middle of the heterojunction interface (the black dash line). ($V_S = 0V$, $V_{GS} = -16V$, $V_{DS} = 900V$).

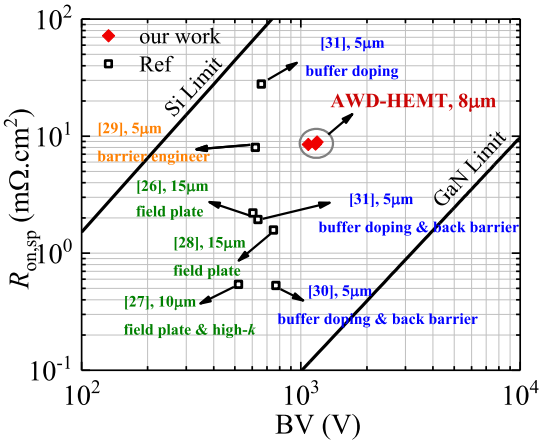

FIGURE 15. The plot of BV versus $R_{on,sp}$ for the AWD-HEMTs and other state-of-art AlGaN/GaN HEMTs.

sustaining-voltage capability. The average electric field in the drift region is as high as 1.48MV/cm. In addition, compared with other HEMTs in published literature, the proposed AWD-HEMT could be fabricated by simply requiring an additional etch process after the standard fabrication process.

V. CONCLUSION

The AlGaN/GaN HEMT with the linearly widened AWD pillars is firstly proposed in this work. By reshaping the charge distribution in the drift region, a more uniform electric field distribution could be obtained. By employing the Gaussian box method, the optimized AWD pillar's width is theoretically obtained and verified by experimental results. The measured results indicate the BV and BFOM of the AWD-HEMTs could achieve a 34.8% and 65.3% improvement against conventional AlGaN/GaN HEMT, respectively. Hence, the DWM technique is a promising approach to achieve high breakdown performance without introducing

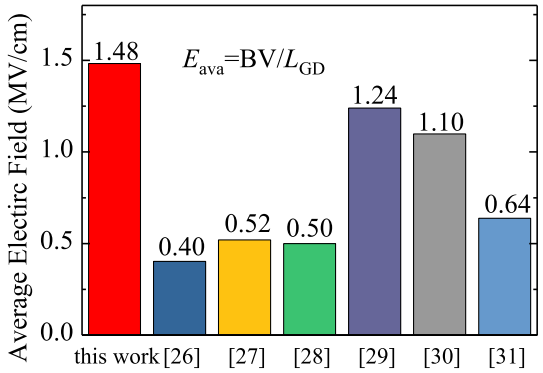

FIGURE 16. The average electric field of the AWD-HEMT and other state-of-art AlGaN/GaN HEMTs.

additional deterioration in performance and complicated fabrication processes.

REFERENCES

[1] X. Ding, Y. Zhou, and J. Cheng, "A review of gallium nitride power device and its applications in motor drive," *CES Trans. Electr. Mach. Syst.*, vol. 3, no. 1, pp. 54–64, Mar. 2019, doi: 10.30941/CESTEMS.2019.00008.

[2] E. Gurpinar, Y. Yang, F. Iannuzzo, A. Castellazzi, and F. Blaabjerg, "Reliability-driven assessment of GaN HEMTs and Si IGBTs in 3L-ANPC PV inverters," *IEEE J. Emerg. Sel. Topics Power Electron.*, vol. 4, no. 3, pp. 956–969, Sep. 2016, doi: 10.1109/JESTPE.2016.2566259.

[3] D.-H. Kim, H. Park, S.-K. Eom, J.-S. Jeong, H.-Y. Cha, and K.-S. Seo, "Ka-band MMIC using AlGaN/GaN-on-Si with recessed high-dual MIS structure," *IEEE Electron Device Lett.*, vol. 39, no. 7, pp. 995–998, Jul. 2018, doi: 10.1109/LED.2018.2834223.

[4] P. Parikh, Y. Wu, and L. Shen, "Commercialization of high 600V GaN-on-silicon power HEMTs and diodes," in *Proc. IEEE Energytech*, Cleveland, OH, USA, Jul. 2013, pp. 1–5, doi: 10.1109/EnergyTech.2013.6645300.

[5] O. Ambacher et al., "Two-dimensional electron gases induced by spontaneous and piezoelectric polarization charges in N- and Ga-face AlGaN/GaN heterostructures," *J. Appl. Phys.*, vol. 85, no. 6, pp. 3222–3233, Mar. 1999, doi: 10.1063/1.369664.

[6] J. P. Ibbetson, P. T. Fini, K. D. Ness, S. P. DenBaars, J. S. Speck, and U. K. Mishra, "Polarization effects, surface states, and the source of electrons in AlGaN/GaN heterostructure field effect transistors," *Appl. Phys. Lett.*, vol. 77, no. 2, pp. 250–252, Jul. 2000, doi: 10.1063/1.126940.

[7] T. Chen, Q. Zhou, D. Wei, C. Dong, W. Chen, and B. Zhang, "Physics-based 2-D analytical model for field-plate engineering of AlGaN/GaN power HFET," *IEEE Trans. Electron Devices*, vol. 66, no. 1, pp. 116–125, Jan. 2019, doi: 10.1109/TED.2018.2873810.

[8] D. Godfrey et al., "Investigation of AlGaN/GaN HEMT breakdown analysis with source field plate length for high power applications," in *Proc. 5th Int. Conf. Devices, Circuits Syst. (ICDCS)*, Coimbatore, India, Mar. 2020, pp. 244–246, doi: 10.1109/ICDCS48716.2020.243589.

[9] B. Liao, Q. Zhou, J. Qin, and H. Wang, "Simulation of AlGaN/GaN HEMTs' breakdown voltage enhancement using gate field-plate, source field-plate and drain field plate," *Electronics*, vol. 8, no. 4, p. 406, Apr. 2019, doi: 10.3390/electronics8040406.

[10] G. Xie et al., "Breakdown-voltage-enhancement technique for RF-based AlGaN/GaN HEMTs with a source-connected air-bridge field plate," *IEEE Electron Device Lett.*, vol. 33, no. 5, pp. 670–672, May 2012, doi: 10.1109/LED.2012.2188492.

[11] L. Nela et al., "Conformal passivation of multi-channel gan power transistors for reduced current collapse," *IEEE Electron Device Lett.*, vol. 42, no. 1, pp. 86–89, Jan. 2021, doi: 10.1109/LED.2020.3038808.

[12] L. Nela et al., "High-performance enhancement-mode AlGaN/GaN multi-channel power transistors," in *Proc. 33rd Int. Symp. Power Semicond. Devices ICs (ISPSD)*, Nagoya, Japan, May 2021, pp. 143–146, doi: 10.23919/ISPSD50666.2021.9452238.

[13] Y. Guo, J. Yao, B. Zhang, H. Lin, and C. Zhang, "Variation of lateral width technique in SoI high-voltage lateral double-diffused metal–oxide– semiconductor transistors using high-k dielectric," *IEEE Electron Device Lett.*, vol. 36, no. 3, pp. 262–264, Mar. 2015, doi: 10.1109/LED.2015.2393913.

[14] J. Yao, Y. Guo, J. Zhang, H. Lin, X. Xia, and Z. Wang, "Novel high-voltage LDMOS with linear graded drift region width," in *Proc. IEEE Int. Conf. Electron Devices Solid-State Circuits (EDSSC)*, Singapore, Jun. 2015, pp. 609–612, doi: 10.1109/EDSSC.2015.7285189.

[15] V. Joshi, S. P. Tiwari, and M. Shrivastava, "Part I: Physical insight into carbon-doping-induced delayed avalanche action in GaN buffer in AlGaN/GaN HEMTs," *IEEE Trans. Electron Devices*, vol. 66, no. 1, pp. 561–569, Jan. 2019, doi: 10.1109/TED.2018.2878770.

[16] N. K. Subramani, J. Couvidat, A. A. Hajjar, J.-C. Nallatamby, and R. Quere, "Low-frequency drain noise characterization and TCAD physical simulations of GaN HEMTs: Identification and analysis of physical location of traps," *IEEE Electron Device Lett.*, vol. 39, no. 1, pp. 107–110, Jan. 2018, doi: 10.1109/LED.2017.2771407.

[17] T. Kabemura, S. Ueda, Y. Kawada, and K. Horio, "Enhancement of breakdown voltage in AlGaN/GaN HEMTs: Field plate plus high-k passivation layer and high acceptor density in buffer layer," *IEEE Trans. Electron Devices*, vol. 65, no. 9, pp. 3848–3854, Sep. 2018, doi: 10.1109/TED.2018.2857774.

[18] B. J. Baliga, "'Gallium nitride devices for power electronic applications," *Semicond. Sci. Technol.*, vol. 28, no. 7, Jul. 2013, Art. no. 74011, doi: 10.1088/0268-1242/28/7/07401.

[19] X. Wang et al., "'Robust SiN_x/AlGaN interface in GaN HEMTs passivated by thick LPCVD-grown SiN_x layer," *IEEE Electron Device Lett.*, vol. 36, no. 7, pp. 666–668, Jul. 2015, doi: 10.1109/LED.2015.2432039.

[20] Y. Dora, A. Chakraborty, L. Mccarthy, S. Keller, S. P. Denbaars, and U. K. Mishra, "High breakdown voltage achieved on AlGaN/GaN HEMTs with integrated slant field plates," *IEEE Electron Device Lett.*, vol. 27, no. 9, pp. 713–715, Sep. 2006, doi: 10.1109/LED.2006.881020.

[21] B. Lu and T. Palacios, "High breakdown (>1500V) AlGaN/GaN HEMTs by substrate-transfer technology," *IEEE Electron Device Lett.*, vol. 31, no. 9, pp. 951–953, Sep. 2010, doi: 10.1109/LED.2010.2052587.

[22] S. Yagi et al., "High breakdown voltage AlGaN/GaN MIS–HEMT with SiN and TiO_2 gate insulator," *Solid-State Electron.*, vol. 50, no. 6, pp. 1057–1061, Jun. 2006, doi: 10.1016/j.sse.2006.04.041.

[23] Y. Alpern, T. Baksht, G. Bunin, E. Capua, Y. Roiter, and D. Rozman, "GaN HEMT with scalable 2.2kV breakdown voltage," in *Proc. IEEE Int. Conf. Microw., Commun., Antennas Electron. Syst. (COMCAS)*, Nov. 2011, pp. 1–3, doi: 10.1109/COMCAS.2011.6105935.

[24] T. Mattila and R. M. Nieminen, "*Ab initio* study of oxygen point defects in GaAs, GaN, and AlN," *Phys. Rev. B*, vol. 54, no. 23, pp. 16676–16682, Dec. 1996, doi: 10.1103/PhysRevB.54.16676.

[25] J.-M. Lee, K.-S. Lee, and S.-J. Park, "Removal of dry etch damage in p-type GaN by wet etching of sacrificial oxide layer," *J. Vac. Sci. Technol. B*, vol. 22, no. 2, p. 479, 2004, doi: 10.1116/1.1645880.

[26] Z. Tang et al., "600-V normally off SiN_x/AlGaN/GaN MIS-HEMT with large gate swing and low current collapse," *IEEE Electron Device Lett.*, vol. 34, no. 11, pp. 1373–1375, Nov. 2013, doi: 10.1109/LED.2013.2279846.

[27] Q. Hu, S. Li, T. Li, X. Wang, X. Li, and Y. Wu, "Channel engineering of normally-ofF AlGaN/GaN MOS- HEMTs by atomic layer etching and high-k dielectric," *IEEE Electron Device Lett.*, vol. 39, no. 9, pp. 1377–1380, Sep. 2018, doi: 10.1109/LED.2018.2856934.

[28] J. Lei, J. Wei, G. Tang, and K. J. Chen, "Reverse-blocking AlGaN/GaN normally-off MIS-HEMT with double-recessed gated Schottky drain," in *Proc. IEEE 30th Int. Symp. Power Semicond. Devices ICs (ISPSD)*, May 2018, pp. 276–279, doi: 10.1109/ISPSD.2018.8393656.

[29] B. Duan, S. Xie, H. Guo, and Y. Yang, "Etched $Al_{0.32}Ga_{0.68}N$/GaN HEMTs with high output current and breakdown voltage (>600 V)," *Micro Nano Lett.*, vol. 13, no. 5, pp. 676–679, May 2018, doi: 10.1049/mnl.2017.0651.

[30] L. Yang et al., "High channel conductivity, breakdown field strength, and low current collapse in AlGaN/GaN/Si δ-doped AlGaN/GaN:C HEMTs," *IEEE Trans. Electron Devices*, vol. 66, no. 3, pp. 1202–1207, Mar. 2019, doi: 10.1109/TED.2018.2889786.

[31] H.-S. Kang et al., "Suppression of current collapse in AlGaN/GaN MISHFET with carbon-doped GaN/undoped GaN multi-layered buffer structure: Suppression of current collapse in AlGaN/GaN MISHFET," *Phys. Status Solidi A*, vol. 212, no. 5, pp. 1116–1121, May 2015, doi: 10.1002/pssa.201431668.